EasyChair Preprint

№ 10165

Identifying Critical Qubits for Gate Implementations in Measurement-Based Quantum Computing

Mohadeseh Azari and Kaushik Seshadreesan

May 15, 2023

Identifying critical qubits for gate implementations in measurement-based quantum computing

Mohadeseh Azari
Department of Informatics and Networked System
University of Pittsburgh
Pittsburgh, PA 15213, USA
moa125@pitt.edu

Kaushik Seshadreesan
Department of Informatics and Networked System
University of Pittsburgh
Pittsburgh, PA 15213, USA
kausesh@pitt.edu

***Abstract*—Measurement-based quantum computation (MBQC) is a powerful technique that relies on multi-qubit entangled cluster states. To realize a universal set of quantum gates, and thus, any quantum algorithm in MBQC, we need to measure the cluster state qubits in suitable measurement bases in proper order, followed by final correction based on the feed-forward of the measurement outcomes. Among photonic qubit architectures, the Gottesman-Kitaev-Preskill (GKP) bosonic continuous-variable (CV) encoding is a great candidate for MBQC. GKP qubits allow for easy application of entangling CZ gates for generating the resource cluster states using beam splitters. However, preparing high-quality, realistic, finite-squeezed GKP qubits can be experimentally challenging. Thus, it is reasonable to expect near-future implementations of GKP-based MBQC on cluster states to contain only a handful of "good" quality GKP qubits. In contrast, other qubits are weakly squeezed GKP qubits or even just squeezed vacuum states. In this paper, we analyze the performance of a universal set of CV gates when a mix of different quality—good and bad—GKP qubits and squeezed vacuum states are used to create the cluster state. By comparing the performance, we identify the critical qubits for each gate in the cluster state for their MBQC realization. Our approach involves comparing the output of the gates with the corresponding expected outputs. We present the logical error rates for the different gate realizations as a function of the GKP squeezing for every combination of good and bad qubits, simulated and determined using Xanadu's Strawberry Fields python library.**

***Index Terms*—measurement-based quantum computation, quantum continuous variables, Gottesman-Kitaev-Preskill qubits**

I. Introduction and Motivation

Measurement-based quantum computation (MBQC) [1] is a promising paradigm that allows us to apply arbitrary quantum computation using entangled resource states, single qubit measurements, and feed-forward. Combining MBQC with bosonic continuous variable (CV) encodings gives us a significant advantage. Lasers and linear optics can easily generate large numbers of bosonic quantum systems or qumodes prepared in multimode Gaussian states in the frequency and temporal domains. So it is easy to generate bosonic 2-d and 3-d Gaussian cluster states of increasing depth [2], [3].

Among encodings of bosonic quantum systems, the GKP qubit encoding [4], [5] is a promising candidate for quantum computation. The GKP qubit's intrinsic error correction properties set it on the highest pedestal among all possible bosonic encodings. However, ideal GKP qubits involve infinite quadrature squeezing and are thus unphysical. Approximate finite squeezed versions of GKP qubits can be prepared using Gaussian boson sampling [6] or photon catalysis [7]. Still, it is experimentally very challenging since the GKP qubit states are highly non-classical, non-Gaussian states [8]. Thus, high-quality finitely squeezed GKP qumodes are aptly expensive in CV photonic quantum computation. In this paper, we pinpoint the most critical nodes within a GKP-qubit cluster and find a possible hierarchy of importance among cluster nodes to implement a universal set of CV quantum gates. Given a set of cluster nodes, an algorithm to implement, and only a handful of good-quality GKP qubits, we can utilize the resources effectively.

The paper is organized as follows. Section II introduces MBQC, the concept of a cluster state, and a simple example of implementing a gate by single qumode measurement. Section III discusses CV quantum computing and the mapping between CV and DV computing, focusing on GKP qubits. Here, we discuss the GKP Wigner function and the advantages of using GKP qubits. Section IV discusses the universal set of CV gates and how to implement MBQC over a CV cluster. After setting the necessary background on CV-MBQC with GKP, Section V elaborates on the simulation design and the result of identifying the critical qubit. We conclude in Section VI.

II. Measurement-based quantum computation

As the name suggests, MBQC conducts quantum computation by applying single-node measurements on an initial n^2-node entangled state called a cluster state, where the nodes are qubits, or more generally, qumodes in the case of CV systems. A cluster state on an $n \times n$ cluster of qubits is a graph state where every node is a qubit prepared in the $|+\rangle$ state (a uniform superposition of the ground and excited states $|0\rangle$ and $|1\rangle$ states, respectively) and every edge is a CZ-gate [9]. MBQC is especially well suited for photonic Gottesman-Kitaev-Preskill (GKP) encoded qubits in qumodes. This is because, with the GKP encoding, we can apply the CZ gate using simple beam-splitters and thus expand the cluster state using only Gaussian operations.

To better illustrate MBQC, we consider a simple example of a two-qubit graph state as shown in Fig. 1. This graph state

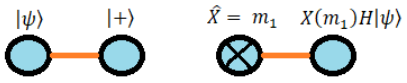

Fig. 1: A simple 2-Qubit graph state. Qubits are pictured as blue nodes, and the CZ gate is the orange line between them. The cross symbol over the qubit represents a measurement. The "$\hat{h}at$" Symbol above the operator represents the measurement axis.

consists of two qubits, initially prepared on the $|\psi, +\rangle$. Then, a CZ gate is applied between the two qubits to generate the final graph state. The first qubit is measured in the X basis, and the outcome is recorded as m_1. In this paper, we decode the eigenvalue 1 as $m_1 = 0$ and the eigenvalue of -1 as $m_1 = 1$. After measuring the first qubit, the conditional state of the second qubit is given by $X(m_1)H\,|\psi\rangle$. The second qubit thus holds the output of the application of the Hadamard gate to the initial state of the first qubit. Note that the Hadamard gate was applied using a single qubit quantum measurement and feed-forward alone [10].

III. CV and GKP Quantum Computation

Discrete variable (DV) quantum computation encodes the state using finite-dimensional quantum systems. [11].

$$|\psi\rangle = \Sigma_i \alpha_i \,|i\rangle\,, \langle i|j\rangle = \delta_{ij} \tag{1}$$

The most basic example is a two-level system, also called a qubit. We can write any pure state of a qubit regarding basis states $|0\rangle\,, |1\rangle$. (Note that $|0\rangle\,, |1\rangle$ can be eigenstates of any unitary). Bosonic CV systems on the other hand are infinite-dimensional quantum systems [12]. The GKP encoding is a particularly robust qubit subspace with good error correction properties that is embedded in a CV system that can be described by the following basis states:

$$\begin{aligned} |0\rangle_{\text{GKP}} &= \Sigma_n \left|q = (2n)\sqrt{\pi\hbar}\right\rangle, \\ |1\rangle_{\text{GKP}} &= \Sigma_n \left|q = (2n+1)\sqrt{\pi\hbar}\right\rangle. \end{aligned} \tag{2}$$

The $|0\rangle_{\text{GKP}}$ and $|1\rangle_{\text{GKP}}$ are superposition of infinitely many position eigenstates, where the $|0\rangle_{\text{GKP}}$ contains states with even multiples of $\sqrt{\pi\hbar}$, i.e., $\left|(2n)\sqrt{\pi\hbar}\right\rangle$, while $|1\rangle_{\text{GKP}}$ has terms of the form $\left|(2n+1)\sqrt{\pi\hbar}\right\rangle$. If we had n copies of the $|0\rangle_{\text{GKP}}$ to measure, the histogram of the recorded result would populate around even numbers (up to a scaling of $\sqrt{\pi\hbar}$), as shown in Fig.2.

A. Wigner function and Finite squeezing

Bosonic CV quantum states can be described by their position and momentum quadrature properties [13]. The set of all the position $|q\rangle$ and momentum $|p\rangle$ eigenstates create the most general way of describing such a system, which satisfies the equations below:

$$\begin{aligned} |q\rangle &= \frac{1}{2\sqrt{\pi}} \int dp e^{-iqp/2}\,|p\rangle\,, \\ |p\rangle &= \frac{1}{2\sqrt{\pi}} \int dq e^{iqp/2}\,|q\rangle\,, \\ \langle q|p\rangle &= \frac{1}{\sqrt{2\pi\hbar}} e^{iqp/\hbar} \end{aligned} \tag{3}$$

$$|\psi\rangle = \int \Psi(x)\,|x\rangle\,dx = \int \Phi(p)\,|p\rangle\,dp \tag{4}$$

Like the Bloch sphere representation of states of a single qubit, the Wigner function or the Wigner quasi-probability distribution is a great way to represent CV states in the phase space (p-q) [14]. Since the Wigner function represents the state density operator and can have negative and positive values, it is called a quasi-probability distribution. Fig. 2 shows the Wigner function of a $|0\rangle_{\text{GKP}}$ state, while Fig. 3 shows its marginal distribution along the q-quadrature. As mentioned in Eq. (2), $|0\rangle_{\text{GKP}}$ is a sum over position basis $|q\rangle$, with values as $(2n)\sqrt{\pi\hbar}$. So in its quadrature distribution, we see a train of delta functions arranged along the position axis, at values of $(2n)\sqrt{\pi\hbar}$ from the origin. In Fig. 3, you also see the effect of finite squeezing on the histogram distribution, with the peak amplitudes decaying as we look farther away from the origin.

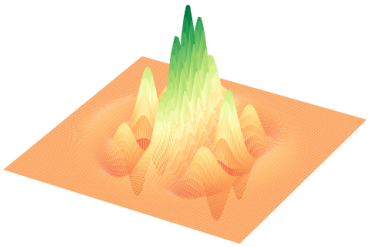

Fig. 2: A 3D Wigner representation of the $|0\rangle_{\text{GKP}}$. As you can see, the distribution has an outer Gaussian envelope, a Gaussian decay as we go farther away from the origin.

B. Pauli operations using displacement

Using one of the favorable properties of GKP qubits, we can apply Pauli operators only by displacing the state along a certain quadrature. For instance, to apply $X(x)\,|0\rangle_{\text{GKP}}$, all we need to do is to displace $|0\rangle_{\text{GKP}}$ along $\hat{q}$ quadrature by $(x)\sqrt{\pi\hbar}$. So to apply the X gate, the displacement should be along $\hat{q}$ quadrature (position is analogous to Pauli Z-basis), and to apply the Z gate, the displacement should be along $\hat{p}$ quadrature (momentum is analogous to Pauli X-basis). We require this discussion in the final section, where we introduce the MBQC circuits and the idea of using displacement on the last qumode as the Pauli correction.

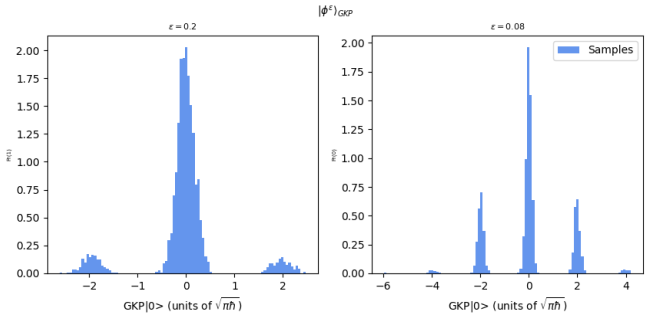

Fig. 3: $\hat{q}$-quadrature distributions of the $|0\rangle_{\text{GKP}}$ state for different values of GKP squeezing. $|0\rangle_{\text{GKP}} = \Sigma_n \left| q = (2n)\sqrt{\pi\hbar} \right\rangle$ so if we measure this state along position quadrature, the outcome values are $m = (2n)\sqrt{\pi\hbar}$. The left figure shows the histogram of the same state but with higher ϵ (meaning being less squeezed). As you can see, by increasing ϵ, the delta function will go toward a Gaussian distribution at $(2n)\sqrt{\pi\hbar}$.

IV. Universal Set of CV Gates

We now review a universal set for CV logic gates [15], [16] and elaborate on each gate separately, where a combination of gates is said to be universal if one can apply any arbitrary unitary operation in terms of elements of the set. Consider the set of gates:

$$Z(p) = e^{ip\hat{q}/\hbar}, P(s) = e^{is\hat{q}^2/2\hbar}, V(\gamma) = e^{i\gamma\hat{q}^3/3\hbar},$$
$$F = e^{i\frac{\pi}{4}(\frac{\hat{q}^2+\hat{p}^2}{\hbar})}, CX(s) = e^{-is(\hat{q}\otimes\hat{p})/\hbar} \quad (5)$$

We analyze implementing these gates in the measurement-based paradigm to track how the measurement bases change upon the qubits that get measured and how to interpret the continuous raw output for feed-forward correction.

First, Fig. 4 shows the general form of applying any single qumode unitary gate denoted as U using MBQC. The initial state of this circuit is a $|\psi+\rangle_{\text{GKP}}$, which goes through a CZ gate to generate the cluster state resource. After preparing the cluster state, one can prove that by measuring the first qumode along the $(U^{\dagger}\hat{p}U)$, the state of the second qumode will be $X(m_1)FU\,|\psi\rangle$, where m_1 is the measurement result of the first qumode, and F is the Fourier gate described in Eq. (5). Thus, we used measurement to perform U-gate on the initial arbitrary state $|\psi\rangle$.

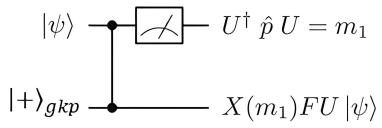

Fig. 4: Applying an arbitrary single qumode gate U in MBQC.

A. Realizing phase gates by MBQC cluster

The Z gate, the quadratic phase gate or P gate, and the cubic phase gate or V gate of Eq. (5) have remarkable similarities in their structure. They are unitaries that are generated by functions of $\hat{q}$ starting from the first order to the third order, respectively. Notice that, unlike the Z and P gates, the V gate is a non-Gaussian operation. Every gate of a structure $U_n(k) = e^{ik\hat{q}^n/n\hbar}$ transforms the momentum quadrature while leaving the position quadrature intact as shown in Eq. (**??**). Their effect on the momentum quadrature ${U_n}^{\dagger}\hat{p}U_n$ can be derived easily using the commutation $[U_n, \hat{p}]$. To find this commutation, first, we should rewrite the U_n in a Taylor series of $\hat{q}^n \forall n$. Eventually, by making use of Eq. (**??**), the measurement axis will change from $\hat{p}$ to $\hat{p} + k\hat{q}^{n-1}$, where n is the power of $\hat{q}$ within the intended gate and k is the scaling of the gate.

$$\begin{aligned} {U_n}^{\dagger}\hat{p}U_n &= \hat{p} + k\hat{q}^{n-1} \\ {U_n}^{\dagger}\hat{q}U_n &= \hat{q} \end{aligned} \quad (6)$$

$$\hat{p}\hat{q}^n + n[\hat{q},\hat{p}]\hat{q}^{n-1} = \hat{q}^n\hat{p} \quad (7)$$

Fig.5 shows the MBQC circuits for the Z, P, and V gates. From the previous discussion within each circuit, the first qumode should be measured along ${U_n(k)}^{\dagger}\hat{p}U_n(k)$, i.e.,

$$\begin{aligned} &\hat{p} + p\hat{1} \text{ for } Z \text{ gate.} \\ &\hat{p} + s\hat{q} \text{ for } P \text{ gate.} \\ &\hat{p} + \gamma\hat{q}^2 \text{ for } V \text{ gate.} \end{aligned}$$

The outcome of this measurement (first qumode measurement) is a continuous real number called m_1. We will discuss the CV measurement output more in Sec. V, but for now, we will take this continuous value m_1 as the X gate scaling to undo the $X(m_1)$ effect on the second qumode. (This is called the feed-forward correction). Remember that this correction is simply a displacement since the m_1 value is known to us.

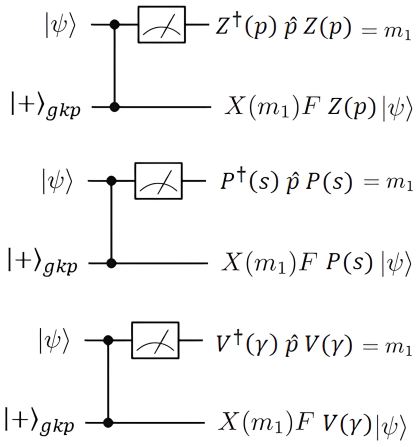

Fig. 5: Z gate (top), the P gate (middle), and the V gate (bottom).

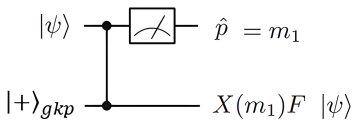

Fig. 6: Measurement-based implementation of the Fourier gate.

B. Realizing Fourier gate by MBQC cluster

Consider the CV rotation gate, $R(\theta) = e^{\frac{i\theta}{2}(\frac{\hat{p}^2+\hat{q}^2}{\hbar})}$ that rotates a quantum state in the (p-q) phase space. The Fourier gate F is a special case of the rotation gate with $\theta = \pi/2$:

$$F = R(\pi/2) = e^{\frac{i\pi}{4}(\frac{\hat{p}^2+\hat{q}^2}{\hbar})}, \tag{8}$$

Figure 7 shows the effect of the Fourier gate on $|0\rangle_{\text{GKP}}$; the blue dots represent positive peaks, and the red ones represent negative peaks. Evidently, the initial $|0\rangle_{\text{GKP}}$ state in the plot on the left (plot A) has been rotated by $\pi/2$ after passing through the Fourier gate, as shown in the plot on the right (plot B). Also, recall that the $|0\rangle_{\text{GKP}}$ is a sum over all the states with $(2n)\sqrt{\pi\hbar}$. If we look at the q-axis in plot A, the odd numbers marginally add to zero (negative peaks cancel out the positive peaks), and only even multiplication of $\sqrt{\pi\hbar}$ remains. So, $|0\rangle_{\text{GKP}}$ has only even values along q quadrature, consistent with Eq. (2). $|+\rangle_{\text{GKP}}$, on the other hand, is a uniform superposition of the $|0\rangle_{\text{GKP}}$ and $|1\rangle_{\text{GKP}}$ states. This means that the plus state would have both the even and odd number of photons, which is $|+\rangle_{\text{GKP}} = (\frac{1}{\sqrt{2}})\Sigma \left|q = (n)\sqrt{\pi\hbar}\right\rangle$. Now look at Fig.7. you can see that the Fourier gate transforms the $|0\rangle_{\text{GKP}}$ to the $|+\rangle_{\text{GKP}}$, which has both the even and odd numbers (they are marginally positive). We note that the Fourier gate is analogous to the discrete variable Hadamard gate.

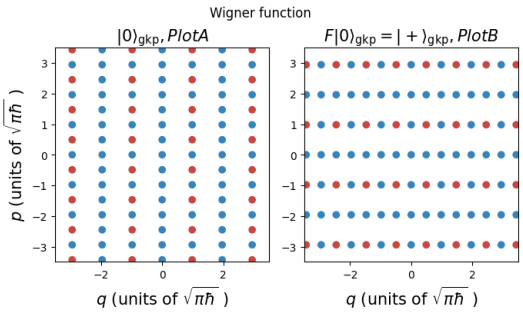

Fig. 7: Input $|0\rangle_{\text{GKP}}$ and output $|+\rangle_{\text{GKP}}$ output of the Fourier gate (the CV analog of the Hadamard gate).

Let us also visualize the MBQC implementation of the P-gate by similarly interpreting the Wigner functions of its input and output. Mathematically speaking, by measuring the first qumode along $P^\dagger \hat{p} P = \hat{p} + \hat{q}$, the second qumode is forced to take the state $X(m_1)FP\,|\psi\rangle$ where m_1 is the measurement result of the first qumode and $|\psi\rangle$ is the initial first qumode state. We can visually verify the same by simulating the action of the gate and plotting the Wigner function of the output. Consider the simple cluster in Fig. 4. Let $|\psi\rangle$ be $P\,|+\rangle_{\text{GKP}}$. So as the initial state, we have $[P\,|+\rangle \otimes |+\rangle]$ (from now on, every encoding is a GKP unless mentioned otherwise). Then we apply CZ-gate to complete the cluster. The state before CZ is: $\frac{1}{\sqrt{2}}[P\,|+\rangle \otimes |0\rangle + P\,|+\rangle \otimes |1\rangle]$ and after the application of the CZ gate is $\frac{1}{\sqrt{2}}[P\,|+\rangle \otimes |0\rangle + ZP\,|+\rangle \otimes |1\rangle]$. Figure. 8 Visualizes the Wigner representations of the $P\,|+\rangle$ and the $ZP\,|+\rangle$ states, respectively, and notice that the grid points are shifted along $\hat{p}+\hat{q}$. To realize the P gate, we then measure the

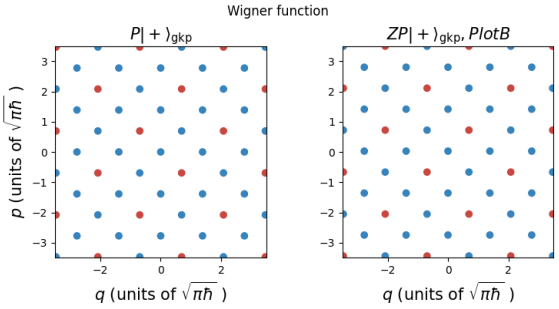

Fig. 8: The effect of the Z-gate on the $P\,|+\rangle_{\text{GKP}}$ state. The initial state has been shifted along $\hat{p} + \hat{q}$ quadrature.

first qumode along $P^\dagger \hat{p} P = \hat{p}+\hat{q}$ and record the measurement result in as m_1 to correct the second qumode $X(m_1)FP\,|\psi\rangle$. We know that $|\psi\rangle$ was initially prepared in the state $P\,|+\rangle$ and so, the second qumode state becomes $X(m_1)FP\,|\psi\rangle = X(m_1)FPP\,|+\rangle = X(m_1)FI\,|+\rangle = X(m_1)\,|0\rangle$. The second qumode is $|0\rangle$ for even results and $|1\rangle$ for odd results. Looking at Fig. 8, we notice that measurement along the $\hat{p} + \hat{q}$ quadrature yields quadrature results in even multiples of a constant factor $(\sqrt{2\pi\hbar})$ for $P\,|+\rangle$ state and odd multiples of the same for $ZP\,|+\rangle$.

C. Realizing two-qumode gate by MBQC cluster

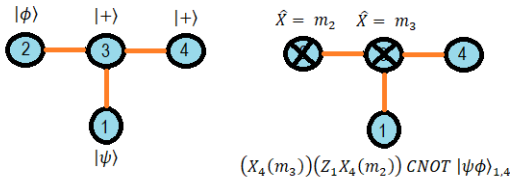

Fig. 9: The MBQC cluster of a two-qubit CX gate. Each node is assigned a number consistent with the state vector representation. The initial state of each qumode (before applying the CZ gate) is written near each node. After applying the CZ gate and performing Pauli $\hat{X}$ or momentum $\hat{p}$ measurement on qumodes 2 and 3, the state of nodes 1,4 will be $CX\,|\psi\phi\rangle_{1,4}$ up to a correction on m_2 and m_3.

So far, we have explored the two-qumode cluster state and how arbitrary single-qumode gates can be realized using suitable single-qumode measurements. However, a universal

gate set requires more than single qumode gates. Any CV universal set needs a two-qumode gate to be complete. The two-qumode gate that we chose in this paper is the Controlled-X gate. This CV-CX gate acts like its DV component; it performs an X-gate on the target node conditioned over the control qumode. Previously, we used a two-qumode cluster for implementing a single-qumode gate. To realize the CX gate, one needs at least four qumodes connected with three CZ operations; Figure. 9 illustrates the qubits as blue nodes and CZ gates as orange lines. Qumodes are numbered from qumode 1 to qumode 4. The control $|\phi\rangle$ and the target $|\psi\rangle$ states sit on qumodes 2 and 1, respectively. The rest of the cluster (qumode 1 and 4) have the $|+\rangle$ state. After initializing the qumodes, the CZ operation finalizes the picture, as shown in the figure. Equations (9) and (10) indicate the system's state before and after the CZ gate.

$$\text{before } CZ \text{ gate} : |\psi, \phi, +, +\rangle \tag{9}$$

$$\text{after } CZ \text{ gate} : \frac{1}{\sqrt{2}}[|\psi, \phi, 0, +\rangle + |\psi', \phi', 1, -\rangle]$$

$$\text{where: } |\psi'\rangle = Z\,|\psi\rangle$$

$$|\phi'\rangle = Z\,|\phi\rangle = \gamma\,|0\rangle + \delta\,|1\rangle \tag{10}$$

After applying the CZ operation, the cluster is ready for computation. To realize the CX gate, one has to measure qumodes 2 and 3 along Pauli $\hat{X}$ or, in the CV picture, along the momentum quadrature $\hat{p}$. (The figure portrays measured nodes as crossed) By recording the measurement results as m_2 and m_3, respectively, we have every tool to complete the MBQC computation. After measurement, qumode 1 and 4 maintain the computation outcome as qumode 1 being the target node and qumode 4 the control node, $|\psi, \phi_{in}\rangle_{1,2}$ goes to $CX\,|\psi, \phi_{out}\rangle_{1,4}$. Remember the final correction in the MBQC picture. Employing measurement feedback is as vital as initializing a cluster. MBQC will only bring purely random products, which is ineffective for any computation if we don't consider the measurement outcomes. Based on the measurement outcomes m_2 and m_3, the state of qumode 1 and 4 go down to one of the following states:

$[\gamma\,|\psi+\rangle + \delta\,|\psi'-\rangle]_{1,4}\,|{+}{+}\rangle_{2,3} +$
$[\gamma\,|\psi+\rangle - \delta\,|\psi'-\rangle]_{1,4}\,|{+}{-}\rangle_{2,3} +$
$[\delta\,|\psi+\rangle + \gamma\,|\psi'-\rangle]_{1,4}\,|{-}{+}\rangle_{2,3} +$
$[\delta\,|\psi+\rangle - \gamma\,|\psi'-\rangle]_{1,4}\,|{-}{-}\rangle_{2,3}$

The following section will discuss the simulation results and circuit implementation. For those readers not familiar with the GKP Maximum Likelihood decoder, please refer to the Appendix.

V. Circuit and Result

This section presents our method of identifying the critical MBQC node for each CV universal gate set element over different GKP damping factors ϵ.

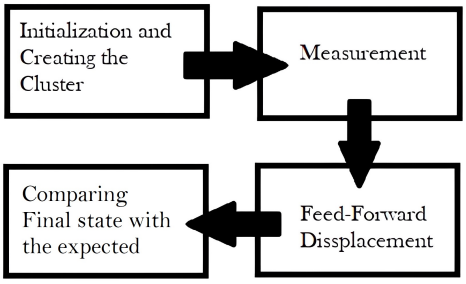

Fig. 10: The overall simulation flowchart. The first three steps are essential for any measurement-based computation. The last step is added to evaluate errors.

The universal set of CV gates [Z-gate, P-gate, V-gate, F-gate, and CX] can be grouped into three cluster types:

Two-qumode cluster state(subgroup a),
Three-qumode cluster state(subgroup b),
Four-qumode cluster state(subgroup c).

Figure. 10 shows the overall simulation flowchart; we need the final step to investigate the error rate. Before diving into the results, let's analyze each Fig. 10 module. In the first module (Initialization and Creating the Cluster), we initialize each qumode in the $|+\rangle_{\text{GKP}}$ state. In the (Measurement) module, we use homodyne measurement defined as $cos(\phi)\hat{q} + sin(\phi)\hat{p}$ to measure each qumode along the required direction. Notice that in subgroup b, since V gate is a non-Gaussian gate, instead of measuring the state $V\,|+\rangle_{\text{GKP}}$ along $\hat{p} + \gamma\hat{q}^2$ (which is not a homodyne measurement) we reverse the effect of the V gate. Then, we have the (Feed-Forward Displacement) module, a displacement operator based on the measurement result from m_q. Eventually, in the (Comparing Final state with the expected), we measure the final state along the appropriate quadrature and repeat this for n number of shots. We must decode and process the final vector to see how often the detection agrees with the anticipated state.

A. Subgroup a

Figure. 11 shows the MBQC implementation of the universal single qumode gates. Based on the simulation error rate, the second GKP qumode is more expensive for universal single-mode gates since the [0.5, 0.005] scenario has less error rate than the [0.005, 0.5] arrangement. This subgroup includes Z-gate, F-gate, and P-gate.

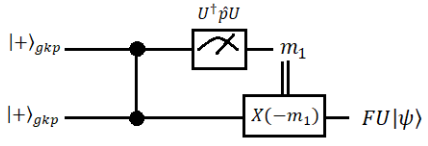

Fig. 11: Two-qumode circuit implementation.

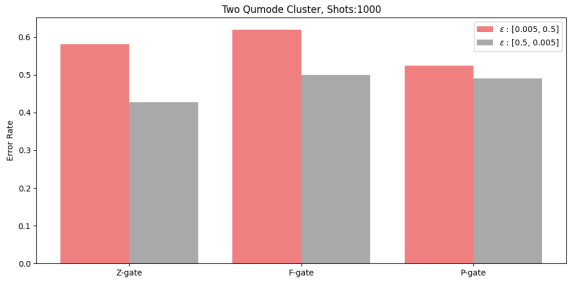

Fig. 12: The bar chart showing the errors across different ϵ. The least error corresponds to the case where the second qumode is the best GKP(has the smaller ϵ)

B. Subgroup b

Subgroup b includes the only non-Gaussian gate in the CV universal set, the V gate. We used the gate injection method mentioned in Ref. [12]. The detail on $V^{\dagger}(m_1, m_2)$ can be found in Ref [17]. Figure. 14 suggests that the second input node $|\gamma\rangle$ has the highest error rate when chosen for the best quality GKP.

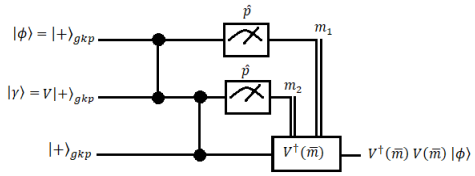

Fig. 13: Three-qumode circuit implementation. The final $V^{\dagger}$ gate is a function of the first two measurement results.

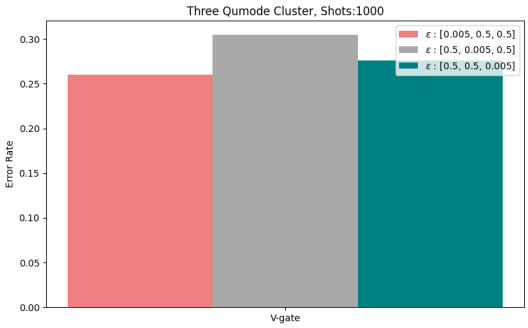

Fig. 14: The bar chart showing the errors across different ϵ. In the three-cluster chain, it is more efficient not to choose the injected input state $|\gamma\rangle$ to hold the best quality GKP.

C. Subgroup c

Subgroup c includes the four-qumode gate, the CX gate. Figure. 15 shows the circuit implementation of this circuit. The previous section has discussed all the circuit details, so that we will go straight to the simulation result. Based on the error rate results, the input nodes have higher error rates when chosen to be the best GKP which means it is more efficient in a CX cluster to use the "good" GKP for the output nodes. The output nodes are our most expensive nodes.

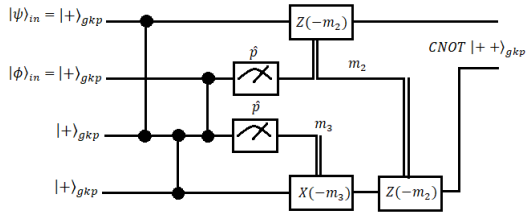

Fig. 15: Four-qumode circuit implementation. The final output nodes are the CX gate applied to the input nodes, measured out.

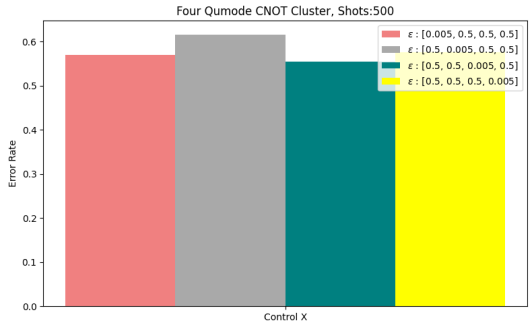

Fig. 16: The bar chart showing the errors across different ϵ. The most error corresponds to the case where the input nodes have the best GKP. Meaning that choosing the output nodes to have good quality GKP would be a clever choice.

VI. Conclusion

The main idea behind our paper was to address this question: If we had a handful of good quality, highly squeezed GKP encoded qubits along with so many poorly squeezed GKPs, how do we most effectively utilize them in the MBQC cluster? We used MBQC to implement each component of the CV universal gate set across "good" and "bad" qualities, and here are the findings: Based on every group cluster's error rate, the simulation suggests that choosing the input node as the excellent quality GKP wastes resources. Note that the assumption was to have only one highly squeezed GKP while other nodes contain poorly squeezed states. The simulation offers to select the output or junction nodes as the best GKP encoding for better error tolerance. Our results thus can be helpful to address the most critical nodes, hence employing the expensive "good" quality GKP resource most efficiently. With this study, we have begun exploring resource-efficient MBQC using GKP qubits. We plan to extend this study and advance our simulation over various input states and gates. One can apply the idea of identifying the critical node with algorithm-specific cluster states mentioned in Ref [18] to find the most vital nodes in a quantum algorithm cluster.

ACKNOWLEDGMENT

MA thanks the Baranger fellowship at the University of Pittsburgh. KPS thanks NSF CIF grant no. 2204985.

REFERENCES

[1] R. Raussendorf, D. E. Browne, and H. J. Briegel, "Measurement-based quantum computation on cluster states," *Physical review A*, vol. 68, no. 2, p. 022312, 2003.
[2] W. Asavanant, Y. Shiozawa, S. Yokoyama, B. Charoensombutamon, H. Emura, R. N. Alexander, S. Takeda, J.-I. Yoshikawa, N. C. Menicucci, H. Yonezawa, and A. Furusawa, "Generation of time-domain-multiplexed two-dimensional cluster state," *Science*, vol. 366, no. 6463, pp. 373–376, Oct. 2019.
[3] O. Pfister, "Continuous-variable quantum computing in the quantum optical frequency comb," *J. Phys. B At. Mol. Opt. Phys.*, vol. 53, no. 1, p. 012001, Nov. 2019.
[4] D. Gottesman, A. Kitaev, and J. Preskill, "Encoding a qubit in an oscillator," *Phys. Rev. A*, vol. 64, no. 1, p. 012310, Jun. 2001.
[5] I. Tzitrin, J. E. Bourassa, N. C. Menicucci, and K. K. Sabapathy, "Progress towards practical qubit computation using approximate gottesman-kitaev-preskill codes," *Physical Review A*, vol. 101, no. 3, p. 032315, 2020.
[6] D. Su, C. R. Myers, and K. K. Sabapathy, "Conversion of gaussian states to non-gaussian states using photon-number-resolving detectors," *Phys. Rev. A*, vol. 100, no. 5, p. 052301, Nov. 2019.
[7] M. Eaton, R. Nehra, and O. Pfister, "Non-Gaussian and Gottesman–Kitaev–Preskill state preparation by photon catalysis," *New J. Phys.*, vol. 21, no. 11, p. 113034, Nov. 2019.
[8] N. Quesada, L. G. Helt, J. Izaac, J. M. Arrazola, R. Shahrokhshahi, C. R. Myers, and K. K. Sabapathy, "Simulating realistic non-gaussian state preparation," *Phys. Rev. A*, vol. 100, no. 2, p. 022341, Aug. 2019.
[9] M. Krishnan Vijayan, A. Paler, J. Gavriel, C. R. Myers, P. P. Rohde, and S. J. Devitt, "Compilation of algorithm-specific graph states for quantum circuits," *arXiv e-prints*, pp. arXiv–2209, 2022.
[10] R. Raussendorf and H. J. Briegel, "A one-way quantum computer," *Physical review letters*, vol. 86, no. 22, p. 5188, 2001.
[11] M. A. Nielsen and I. Chuang, "Quantum computation and quantum information," 2002.
[12] C. Weedbrook, S. Pirandola, R. García-Patrón, N. J. Cerf, T. C. Ralph, J. H. Shapiro, and S. Lloyd, "Gaussian quantum information," *Reviews of Modern Physics*, vol. 84, no. 2, p. 621, 2012.
[13] W. P. Schleich, *Quantum optics in phase space*. John Wiley & Sons, 2011.
[14] T. Tilma, M. J. Everitt, J. H. Samson, W. J. Munro, and K. Nemoto, "Wigner functions for arbitrary quantum systems," *Physical review letters*, vol. 117, no. 18, p. 180401, 2016.
[15] S. Sefi and P. Van Loock, "How to decompose arbitrary continuous-variable quantum operations," *Physical review letters*, vol. 107, no. 17, p. 170501, 2011.
[16] T. Kalajdzievski and N. Quesada, "Exact and approximate continuous-variable gate decompositions," *Quantum*, vol. 5, p. 394, 2021.
[17] M. Gu, C. Weedbrook, N. C. Menicucci, T. C. Ralph, and P. van Loock, "Quantum computing with continuous-variable clusters," *Physical Review A*, vol. 79, no. 6, p. 062318, 2009.
[18] M. K. Vijayan, A. Paler, J. Gavriel, C. R. Myers, P. P. Rohde, and S. J. Devitt, "Compilation of algorithm-specific graph states for quantum circuits," *arXiv preprint arXiv:2209.07345*, 2022.
[19] K. Fukui, "High-threshold fault-tolerant quantum computation with the gkp qubit and realistically noisy devices," *arXiv preprint arXiv:1906.09767*, 2019.

APPENDIX

We dedicated this appendix to the GKP Maximum Likelihood decoder. The GKP Wigner representation is an arrangement of delta functions in the phase space where marginal distributions along $\hat{q}$ / $\hat{p}$ encode the Pauli Z / X eigenstates, respectively. Equation. (2) shows the $|0\rangle_{\text{GKP}}$ and $|1\rangle_{\text{GKP}}$ states. Without loss of generality, let us focus on $|+\rangle_{\text{GKP}}$. What will be the result m, if we measure $|+\rangle_{\text{GKP}}$ along $\hat{q}$? As previously examined, we will see k number of photons where $k = (n)\sqrt{\pi\hbar}$ and duo to the finite squeezing n follows a Gaussian-like probability distribution. Thus, detecting high numbers is less likely in the result.

$|+\rangle_{\text{GKP}} = \frac{1}{\sqrt{2}}[|0\rangle_{\text{GKP}} + |1\rangle_{\text{GKP}}]$ which means half of the time $k = (2n)\sqrt{\pi\hbar}$ and the other half of the time it is $(2n+1)\sqrt{\pi\hbar}$. So if one measure the state $|+\rangle_{\text{GKP}}$ and look at its outcome k, the state records as $|0\rangle_{\text{GKP}}$ if k was even and as $|1\rangle_{\text{GKP}}$ if k was odd. This decision would be flawless if ideal GKPs were viable. However, energy is finite, so the perfect delta function is unphysical. The delta picks at each value would instead obey a normal distribution. Figure. 17 shows the histogram of $|+\rangle_{\text{GKP}}$ measurement results for 2500 shots. Since the picks follow a Gaussian, we must set thresholds for each value. For instance, values in $[-0.5\sqrt{\pi\hbar}, 0.5\sqrt{\pi\hbar}]$ range are decoded as 0, values within $[0.5\sqrt{\pi\hbar}, 1.5\sqrt{\pi\hbar}]$ are decoded as $\sqrt{\pi\hbar}$ and so on. So in our $|+\rangle_{\text{GKP}}$ example, when one measures $|+\rangle_{\text{GKP}}$ along $\hat{q}$ and obtains the outcome k, by using Maximum Likelihood Estimate (MLE) [19], if k was within the threshold of the even/odd numbers, it records $|0\rangle_{\text{GKP}}$ and $|1\rangle_{\text{GKP}}$ respectively. Look closely at Fig. 17; you can notice the overall Gaussian envelope along with the normal distribution at each value.

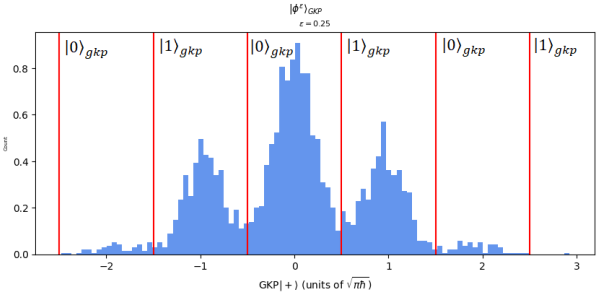

Fig. 17: The histogram of the $|+\rangle_{\text{GKP}}$ for 2500 number of shots. Thresholds are red vertical lines